Ameboid cell migration through regular arrays of micropillars under confinement

Zeinab Sadjadi,[1,2,*] Doriane Vesperini,[3] Annalena M. Laurent,[3] Lena Barnefske,[4] Emmanuel Terriac,[3] Franziska Lautenschläger,[2,3] and Heiko Rieger[1,2,4]

[1]Department of Theoretical Physics, Saarland University, Saarbrücken, Germany; [2]Centre for Biophysics, Saarland University, Saarbrücken, Germany; [3]Department of Experimental Physics, Saarland University, Saarbrücken, Germany; and [4]Leibniz-Institute for New Materials, Saarbrücken, Germany

ABSTRACT   Migrating cells often encounter a wide variety of topographic features—including the presence of obstacles—when navigating through crowded biological environments. Unraveling the impact of topography and crowding on the dynamics of cells is key to better understand many essential physiological processes such as the immune response. We study the impact of geometrical cues on ameboid migration of HL-60 cells differentiated into neutrophils. A microfluidic device is designed to track the cells in confining geometries between two parallel plates with distance h, in which identical micropillars are arranged in regular pillar forests with pillar spacing e. We observe that the cells are temporarily captured near pillars, with a mean contact time that is independent of h and e. By decreasing the vertical confinement h, we find that the cell velocity is not affected, while the persistence reduces; thus, cells are able to preserve their velocity when highly squeezed but lose the ability to control their direction of motion. At a given h, we show that by decreasing the pillar spacing e in the weak lateral confinement regime, the mean escape time of cells from effective local traps between neighboring pillars grows. This effect, together with the increase of cell-pillar contact frequency, leads to the reduction of diffusion constant D. By disentangling the contributions of these two effects on D in numerical simulations, we verify that the impact of cell-pillar contacts on cell diffusivity is more pronounced at smaller pillar spacing.

SIGNIFICANCE   Cell migration through environments with complex topographical features, such as extracellular matrices and confined tissue, plays a crucial role in various physiological processes. It is important to understand how confinement and the presence of obstacles influence cell migration. We study ameboid cell migration in regular arrays of micropillars while the cells are also squeezed vertically between two parallel plates. Upon further squeezing, we find that the migration velocity is not affected but that the cells lose control of their direction of motion. We also demonstrate how combined effects of scattering from pillars and cell-pillar interactions govern cell diffusivity in a weak lateral confinement regime. Besides basic research, our results should be considered in practical applications such as design of topotaxis devices.

INTRODUCTION

Cell migration is essential for various physiological processes such as wound healing, morphogenesis, and immune responses (1–3). Cells and other organisms can adapt their migration in response to different environmental cues such as gradients of chemical, electrical, or mechanical signals. Recently, the ability of migrating cells to sense and follow topographic environmental cues has attracted attention, the so-called *topotaxis* (4,5). Similar to other taxis phenomena,

variations in topographic features of the surrounding environment—such as the spatial arrangement of obstacles, degree of lateral confinement, surface topography, etc.—can be exploited by biological organisms to navigate more efficiently (5–10). The idea of topotaxis can be utilized to conduct the migration of cells, e.g., by tuning spatial confinements or designing favorable arrangements of obstacles. To achieve an efficient topotaxis, however, a detailed understanding of the impact of crowding and confinement on different cell migration modes is required, which is currently lacking.

Ameboid migration is a fast cell migration mode that relies on friction instead of adhesion (6,11,12). Various cell types exhibit this mode of migration, among which immune

cells have been of particular interest (13–16). One of the main functions of immune cells is to detect pathogens by exploring confined tissues and extracellular matrices with different degrees of confinement. Although migration through such environments was mimicked in different ways *in vitro* (17–19), arrays of micropillars have been recently employed to systematically study the role of confinement on cell migration (5–7,20); denoting the pillar spacing with e and the typical cell size with L, these studies have considered strong lateral confinements $\left(0 < \frac{e}{L} \lesssim 1.5\right)$, where the cell is often in simultaneous contacts with more than one pillar and experiences a directed pillar-to-pillar type of motion. In contrast, ameboid migration under weak lateral confinement $\left(1.5 \lesssim \frac{e}{L}\right)$ has been poorly studied. In this regime, the cell cannot be in simultaneous contact with more than one pillar, and it is unclear how the cell-pillar interactions affect cell migration. Understanding the cell dynamics in this regime is of importance toward practical applications such as design of topotaxis devices.

Scattering from obstacles—as, e.g., observed for microalgae by pushing their flagella against obstacles (21–23)—randomizes the trajectory and reduces the diffusion constant (24–32). As another possible type of interaction with obstacles, moving biological agents may be temporarily captured near obstacles. Such events have been reported for swimming bacteria (33–35), killer cells (36), and migrating cells in pillar forests (at highly dense regimes of pillars) (5,20). The combined effects of scattering from and trapping by obstacles on the dynamics of migrating cells has not been well understood yet.

When confining the cells that migrate purely in the ameboid mode (such as immature dendritic cells (16,37)) to move between two parallel plates, migration only starts if the vertical confinement h between the plates is small enough; otherwise, the cells remain immobile. It was reported in (38) that the cell velocity reduces upon further squeezing the cell (i.e., decreasing h). Nevertheless, there is very little experimental information on how the degree of vertical confinement h influences the cell dynamics in the ameboid migration mode.

In this work, we study the topographical influence of the environment on in vitro ameboid cell migration in regular arrays of micropillars. Our differentiated HL-60 cells move between two parallel plates in the presence of cylindrical pillars in the weak lateral confinement regime. We observe that the cells spend a finite amount of time in the vicinity of pillars, with a mean cell-pillar contact time τ_c that is independent of the vertical confinement h and the pillar spacing e. By decreasing h, we interestingly find that the cell velocity is not affected, while the persistence reduces. We also find that the diffusion constant D of cells reduces with decreasing the lateral confinement e. To demonstrate how trapping by and scattering from pillars influence D, we perform numerical simulations. Random-walk models can be a powerful tool to untangle complex cell migratory behavior from the experimental data. Stochastic two-state models consisting of altering phases of fast and slow motions, such as run-and-tumble or run-and-pause dynamics, have been widely employed to describe locomotive patterns in biological systems (39–44). A proper numerical model, however, needs to be capable of capturing the topographical features of the problem. Our simulations reveal that the impact of cell-pillar contacts on D is pronounced at smaller pillar spacing e but becomes negligible in the limit of large e.

MATERIALS AND METHODS

Cells

We used HL-60 cells, an acute promyelocytic cell line, which we differentiated into neutrophils. This cell line has been used extensively in the literature as a model for neutrophil migration (18,45). The cell line was cultured in Roswell Park Memorial Institute medium (RPMI-1640, Gibco) supplemented with 10% fetal bovine serum (Thermo Fisher Scientific, Waltham, MA, USA), 1% Glutamax (Thermo Fisher Scientific), and 1% penicillin/streptomycin (Gibco). For differentiation of HL-60 cells into neutrophils we applied a standard protocol (46) using 1.3% DMSO (Thermo Fisher Scientific) for 3 days before performing the experiments.

Pillar forest geometries

The pillar forest chambers were designed with Autodesk Inventor (47). The design contains a cell loading inlet and a migration area, where cells were tracked (see Fig. 1). This tracking area consists of six vertically stacked
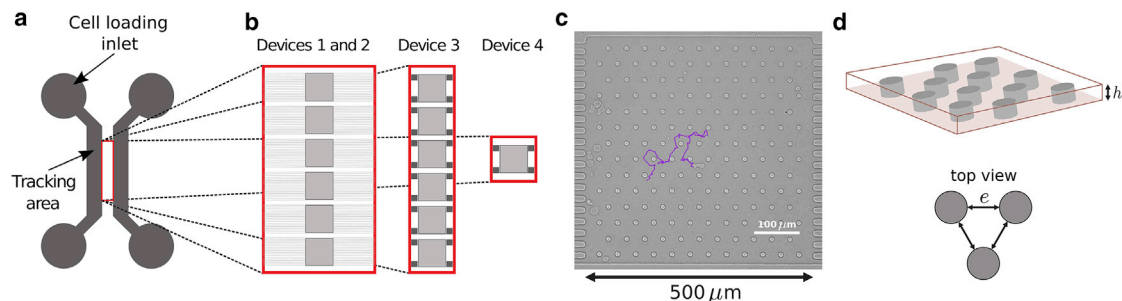

FIGURE 1 Sketch of the experimental devices. (*a*) General view of the cell loading channels. (*b*) Zoom of the tracking area for each device. (*c*) Example of the bright-field image of device D3, in which a typical cell track is shown. (*d*) Definition of the pillar spacing e and the vertical confinement h. To see this figure in color, go online.

chambers, each with a dimension of $500 \times 500 \ \mu m^2$. The chambers were filled with pillars with a diameter $d (\sim 13 \ \mu m)$ and a pillar spacing e, varied in the range $15 \ \mu m \leq e \leq 50 \ \mu m$. The resulting chambers had different pillar densities, named dense, intermediate, and sparse; see Table 1 for details. The pillars were organized in a triangular lattice. The vertical confinement h, i.e., the plate-plate distance, was determined by the pillar height. Three sets of devices with increasing $h \in \{3.5, 5.0, 6.0 \ \mu m\}$ were named D1, D2, and D3, respectively. We had an extra-dense device D4 with $e = 5 \ \mu m$ and $h = 4 \ \mu m$, which we named packed device. The detailed geometrical information of the pillar forests is summarized in Table S1.

Production of the wafers

The tracking area of the devices D1 and D2 consisted of six chambers, connected to the cell loading channel of 900 μm width and 50 μm height via 20 small channels of 10 μm width and 3.5 or 5 μm height (see Fig. 1). The devices resulting from designs D1 and D2 were fabricated using the standard photolithography technique, with processing guidelines from Microchem, in two steps. Briefly, a 4-inch silicon wafer was covered with a first layer of SU8-3005 (Microchem, Round Rock, TX, USA) to produce the tracking area, spin coated at 500 Rpm for 15 s followed by 4,000 Rpm for 40 s or 3,000 Rpm for 30 s, to get the desired heights (respectively, 3.5 and 5 μm). Then, the wafer was soft baked for 2 min at 95°C and exposed to UV light (UV-KUB-2, Kloe, Saint-Mathieu-de-Tréviers, France) through a mask with an illumination of 50% for 7 and 8 s, respectively. The wafer was then postbaked for 2 min at 95°C, developed in a developer solution for 1 min, and rinsed with isopropanol (CAS number 67-63-0). The second layer of the master fabrication, which gives rise to the cell loading inlets and channels, was produced using SU8-3025 (Microchem), spin coated at 500 Rpm for 15 s and 1500 Rpm for 45 s. Then, the wafer was soft baked for 2 min at 95°C and exposed to UV light through a mask with an illumination of 50% for 32 s. The wafer was then postbaked for 5 min at 95°C, developed in a developer solution for 8 min, and rinsed with isopropanol. The tracking area of devices D3 and D4 consisted of six chambers and one chamber, respectively, which were connected to the cell loading channel of 900 μm width and 100 μm height via square channels of $100 \times 100 \times 100 \ \mu m^3$ placed at each corner of each chamber (see Fig. 1). They were printed by two-photon lithography using a Nanoscribe GT+ (Nanoscribe, Eggenstein-Leopoldshafen, Germany) with IP-S resin (Nanoscribe) on ITO-coated glass substrates using a 25× objective. A laser intensity of 150 mW and a writing speed of 100 mm/s was used to write our design into the resin. For development of the devices, we washed them with PGMEA (CAS number 108-65-6), which we then exchanged with isopropanol. Next, we postcured the device for 5 min under 200 W UV radiation (OmniCure Series 1500, IGB-Tech GmbH). The samples were carefully dried under nitrogen stream. In order to reduce printing time, the migration chambers were printed in high accuracy, but the cell loading inlets, which require less accuracy, were printed with a shell and scaffold printing mode, which was faster, but a postcuring process was necessary. We note that a precise control of both h and d was challenging with our available techniques. With two-photon lithography, we had a precise control on d at large values of h, but it was not accurate enough to produce devices with $h \lesssim 5.0 \ \mu m$. With photolithography, we had a much better resolution in height but lost control over d. Since h was a key parameter for us, we precisely controlled h and let d vary.

Production of the microfabricated devices

Microfabricated devices were replica molded into silicone rubber (RTV615, Momentive Performance Materials, Waterford, NY, USA; CAS numbers 556-67-2 and 540-97-6) using soft lithography. Briefly, the silicon rubber was cast onto the wafers, degassed, and polymerized at 75°C for 2 h. The resulting devices were peeled off and sealed in 35-mm glass-bottom cell culture dishes (World Precision Instruments, Sarasota, FL, USA) using plasma surface activation.

Experimental setup

Prior to the experiment, the assembled migration chambers were coated with 100 $\mu g.mL^{-1}$ poly-L-lysine (20 kDa) (CAS number 25988-63-0) grafted with polyethylene glycol (2 kDa) (PLL-PEG) (Sigma-Aldrich, St. Louis, MO, USA; CAS number 25322-68-3) for 30 min at room temperature to prevent adhesion. For tracking purposes, cell nuclei were stained with 200 $ng.mL^{-1}$ Hoechst 34580 (Sigma Aldrich; CAS number 911004-45-0) for 30 min before being placed into the cell loading channel with a concentration of $5 \times 10^3 \ cells.mL^{-1}$. When cells started to fill the migration chamber, the rest of the cell culture dish was filled with RPMI medium (RPMI-1640, Gibco) and kept at 37°C for at least 30 min before starting the experiment to reduce nutrient gradients within the migration chamber. Moreover, we kept the chip including the cells for 1 h in the incubator before the experiment. Additionally, the devices were slightly permeable, which further counteracted gradients. Fluorescent images of cell nuclei and bright-field images of the pillar chamber were recorded using an EMCCD camera (Andor Technology, Belfast, Northern Ireland, UK) with a physical pixel size of 0.65 μm and a binning of 2×2, mounted on a Nikon Eclipse Ti epifluorescent microscope, at a 10× magnification and 0.5 numerical aperture over 12 h with a frame rate of 2 min. The cells were kept at constant atmosphere of 37°C and 5% CO_2 (Okolab, Pozzuoli NA, Italy) during the entire experiment. To minimize bleaching effect, the exposure times were kept at 100 ms for the fluorescent images and 20 ms for the bright-field images.

Data analysis

Cell trajectories were analyzed using ImageJ plugin TrackMate. We excluded the trajectories of dying and dividing cells. The maximum tracking time was 700 min; however, we excluded the first 100 min of all tracks until the cells reached the bulk of the chambers. Since the cells entered the camera field at different times, we shifted the starting time of all trajectories to have all cells starting at the same time, which is $t = 100$ min in real time in our experiments. Each trajectory consisted of a set of (x, y) positions, recorded after successive time intervals $\Delta t = 2$ min. Every two successive recorded positions were used to calculate the instantaneous velocity and every three of them to extract the local turning angle φ. A small φ corresponds to a highly persistent motion, i.e., moving nearly along the previous direction of motion. On the other hand, φ approaches π when the direction of motion is nearly reversed. We quantified the local cell persistence with $\cos \varphi$, ranging from 1 for forward motion to -1 for backward turning. The mean local persistence was then obtained as $\mathscr{R} = \langle \cos \varphi \rangle$ (48,49), with $\mathscr{R} \in [-1, 1]$. Note that the cell persistence can be equivalently quantified by the persistence length ℓ_p, which is related to $\mathscr{R}$ via $\mathscr{R} \propto e^{-\ell/\ell_p}$ with ℓ being the mean step size of the walker (50,51). All statistical quantities were calculated for each geometry by adding up all trajectories in the corresponding experiments. The number of cell trajectories analyzed in each experiment as well as the number of experiments performed for each geometry are given in the caption of figures and summarized in Table S2 (also see the list of the parameters used in the article in Table S3). The mean-square displacement (MSD) was calculated as $MSD(t) = \langle r(t)^2 \rangle - \langle r(t) \rangle^2$, where $\langle \cdots \rangle$ is the average over all cell trajectories in one chamber.

TABLE 1 Pillar spacing e and vertical confinement h in μm for each device and pillar density

Device	D1		D2		D3	
Parameter	e	h	e	h	e	h
Sparse (T1)	49	3.5	47	5	45	6
Intermediate (T2)	29	3.5	28	5	25	6
Dense (T3)	18	3.5	17	5	15	6

Simulation method

Monte Carlo simulations were performed to study cell migration through a two-dimensional medium consisting of circular pillars. To mimic each experiment, the corresponding experimental distributions of velocity and persistence, the setup dimensions, and the position and size of pillars served as input for simulations. By considering a two-dimensional simulation box, the effect of the vertical confinement h of the microfluidic device on cell migration was implicitly taken into account through the h dependence of the persistence of cells. An ensemble of 10^5 persistent random walkers started their motion from a random position on the left border (as in the experiments) and with a random shooting angle into the simulation box with periodic boundary conditions. The random walkers were disks with a diameter of 10 μm, i.e., of the order of the typical cell size. To move the walker after each time step $\Delta T = 2$ min, the new velocity and direction of motion were extracted from the input velocity and turning angle distributions. Upon encountering a pillar, we assumed that a contact occurs when the distance between the surfaces of the walker and the pillar drops below a threshold distance $\delta = 2$ μm. The walker was reflected from the pillar through a specular reflection. We considered two models for the walker-pillar interaction: with and without a contact time τ_c. In the model with contact time, we paused the walk for a time τ_c before being reflected. See Fig. S1 for details of the simulation algorithm. We also performed additional simulations with a uniform velocity distribution around the overall mean value $v = 3.5$ $\mu m/min$ of experiments and a uniform turning-angle distribution corresponding to $\mathcal{R} = 0$. The simulation box was 500×500 μm, consisting of a lattice of circular obstacles with diameter $d = 15$ μm. The pillar spacing was varied, and we used an ensemble of 10^5 persistent random walkers, which started their motion from a random position with a random direction.

RESULTS

In order to understand the influence of vertical confinement and pillar spacing on ameboid cell migration, we use three devices, D1, D2, and D3, with the plate-plate distance $h = 3.5$, 5, and 6 μm, respectively. Each of these devices contains pillars of diameter d arranged on triangular lattice configurations with different pillar spacing e (see the materials and methods section, Table 1, and Fig. 1 for details of geometrical properties). The mean diameter of differentiated HL-60 cells in our experiments is around 10 μm, which is smaller than the pillar spacing in all chambers of devices D1, D2, and D3. However, we also construct a highly dense device D4 with $e = 5$ μm and $h = 4$ μm; thus, here the cells are highly confined both vertically and laterally. Cells enter the chambers from one side and move through pillars.

Influence of vertical confinement *h*

The distribution $P(v)$ of instantaneous cell velocity v in different chambers is presented in Fig. 2 *a*. The tail of $P(v)$ decays faster than exponential for all chambers, and no trend can be observed in different devices or in terms of pillar spacing. We also analyze the local turning angle φ of cells. The turning-angle distribution $P(\varphi)$ is shown in Fig. 2 *b* for different chambers. In all cases, $P(\varphi)$ develops two peaks around $\varphi = 0$ and π, reflecting that the motion in near-forward or -backward directions are more probable.
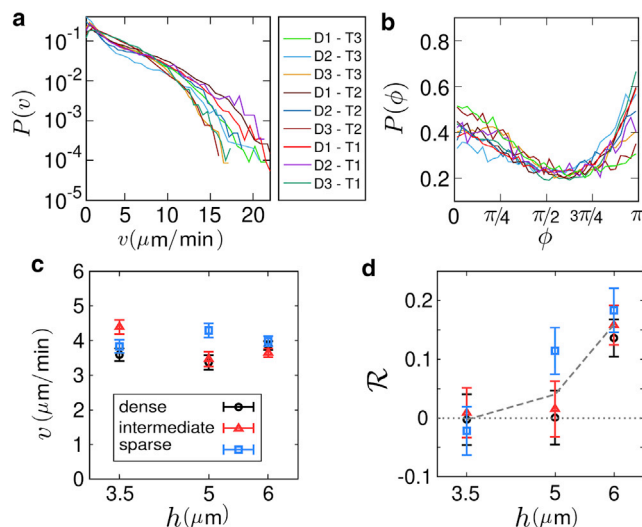

FIGURE 2 (*a*) Velocity distribution $P(v)$ in log-lin scale for all configurations. The characteristics of each configuration are given in Table 1. The number of cell tracks for three pillar spacing (T1, T2, T3) of devices D1, D2, and D3 are (144, 79, 130), (30, 95, 64), and (50, 25, 56), respectively. The corresponding number of independent experiments performed for devices D1 to D3 are (10, 9, 11), (5, 6, 4), and (4, 5, 6), respectively. (*b*) Turning-angle distribution $P(\varphi)$ for all configurations. All line colors are as in (*a*). (*c* and *d*) Mean velocity $v(c)$ and mean local persistence $\mathcal{R}$ (*d*) of cells in terms of vertical confinement h for different pillar spacing h. The error bars indicate the standard deviation *std*. To see this figure in color, go online.

Fig. 2 *c* shows the mean instantaneous velocity v in terms of the vertical confinement h for different choices of pillar spacing e. It is evident that v does not systematically depend on h or e.

Next, we quantify the mean local persistence of cells in each chamber by the dimensionless parameter $\mathcal{R} = \langle \cos \varphi \rangle$ (48), where $\langle \cdots \rangle$ denotes averaging over all cell trajectories in one chamber. $\mathcal{R}$ ranges from -1 for pure localization to 0 for diffusion and 1 for ballistic motion (see the materials and methods section for data analysis details). Fig. 2 *d* shows the mean local persistence $\mathcal{R}$ versus h at different pillar spacings. $\mathcal{R}$ reduces with decreasing h in all pillar densities and eventually reaches $\mathcal{R} \simeq 0$ at $h = 3.5$ μm, where the cells move nearly diffusively. See also Videos S1 and S2 and Fig. S2 for a comparison between the cell trajectories at small and large values of h. Thus, our noteworthy observation is that under a stronger vertical confinement, cells lose their persistence while still preserving their velocity.

Influence of pillar spacing *e*

In addition to the degree of vertical confinement between the parallel plates, cell dynamics is also affected by the lateral confinement imposed by pillars. While the regime of strong lateral confinement has been previously studied (5–7,20), here we are interested in the weak lateral

confinement regime, where the cells cannot be in simultaneous contact with more than one pillar. To quantify the impact of the pillar spacing e on the dynamics of cells, we measure the MSD and the diffusion constant D in different chambers.

To study the effect of pillar spacing e on the MSD, we note that the extracted MSD from experiments reflects the combined effects of e, cell velocity, and cell persistence. The mean local persistence and the mean and variance of the cell velocity vary from experiment to experiment; thus, a direct comparison of the MSD curves is not informative. It is known that the MSD of a persistently moving object in a uniform space depends on the velocity moments and persistence as (52)

$$\text{MSD}_p(t) \sim \left(\langle v^2 \rangle + \langle v \rangle^2 \frac{2\mathcal{R}}{1 - \mathcal{R}} \right) t. \quad (1)$$

To be able to compare the MSD from different experiments, we rescale them by $\text{MSD}_p(t)$ from Eq. 1 using the corresponding experimental values. The resulting rescaled MSD ($\widetilde{\text{MSD}}(t) = \text{MSD}(t)/\text{MSD}_p(t)$), shown in Fig. 3, a–c, reveals that decreasing the pillar spacing (i.e., from T1 to T3) leads to a lower diffusivity in all devices. We note that this trend is also visible in the behavior of the unscaled diffusion constant D versus e in Fig. 3 d and even by looking at the sample cell trajectories at different e shown in

Figs. S3 and S4 a (see also Videos S3 and S4 to compare the cell trajectories in devices with the same h but small or large values of e); however, the effects of velocity and persistence are also present in such plots, preventing from isolating the impact of e on the cell dynamics.

In the following, we identify two mechanisms responsible for the reduction of cell diffusivity upon decreasing e: 1) formation of effective local traps between adjacent pillars in the weak lateral confinement regime and 2) being temporarily captured near pillars.

Escape from effective local traps

We plot in Fig. 4 a the cell persistence $\mathcal{R}$ as a function of pillar spacing e for different values of h. The slight reduction of $\mathcal{R}$ with decreasing e suggests that the cells are scattered from pillars more frequently at small pillar spacing. Scattering from pillars in the weak lateral confinement regime leads to the formation of effective local traps between adjacent pillars. To quantify the strength of trapping, we calculate the mean escape time t_{esc} as the time spent by the cell in the area confined between adjacent pillars (see the *gray zone* in Fig. 4 b and (5)). Indeed, t_{esc} is the time which takes for a cell to escape a local trap formed by adjacent pillars and move to the next trap. Fig. 4 c shows that the decrease of e leads to a shorter t_{esc}, but it also reduces the area of each trap zone $A_{\text{trap}}^{\text{T}} = \frac{\sqrt{3}(e+d)^2}{4} - \frac{\pi d^2}{8}$. Thus, we rescale the escape time to A_{trap} to obtain the escape time per unit
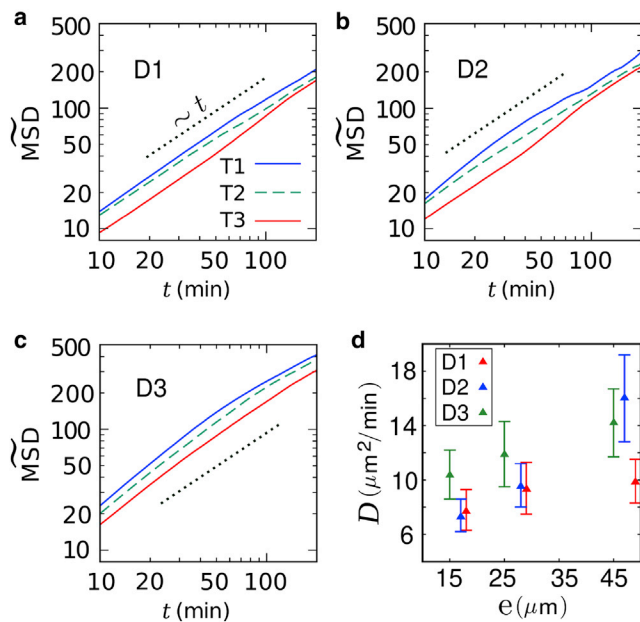

FIGURE 3 (*a*–*c*) Time evolution of the scaled MSD of cells in devices D1 to D3 with different pillar spacing T1 to T3. The dotted lines represent normal diffusion and serve as a guide to the eye. (*d*) Diffusion constant D of cells in terms of pillar spacing e in different devices. The error bars indicate the standard deviation. The numbers of independent experiments and analyzed tracks are given in the caption of Fig. 2. To see this figure in color, go online.
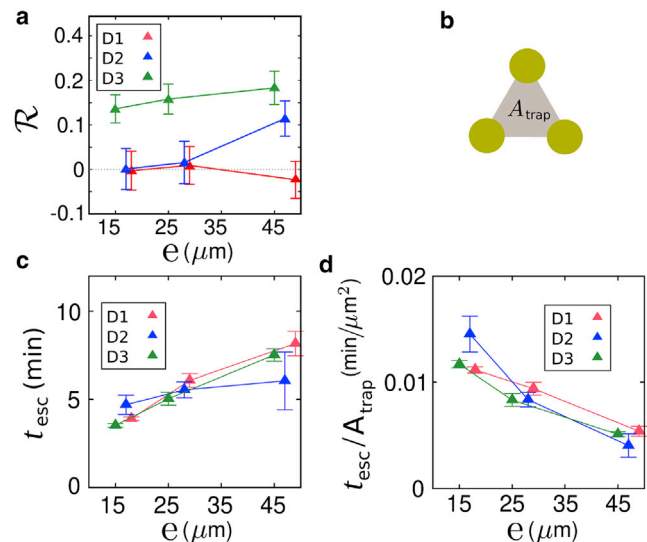

FIGURE 4 (*a*) Mean local persistence $\mathcal{R}$ of the cells versus pillar spacing e for different devices. (*b*) Schematic drawing of the trap zone (*gray region*), i.e., the region confined between adjacent pillars. The corresponding area is denoted with A_{trap}. (*c*) Mean escape time t_{esc} versus e for different devices. (*d*) Mean escape time, scaled by the trap zone area A_{trap}, versus e for different devices. The error bars indicate the standard deviation. The numbers of independent experiments and analyzed tracks are given in the caption of Fig. 2. To see this figure in color, go online.

area. The resulting plot in Fig. 4 *d* verifies that the decrease of *e* enhances the rescaled escape time and, thus, strengthens the trapping effect.

Cell-pillar contacts

To characterize the cell-pillar interaction, we measure the time spent by cells in the vicinity of pillars. A few examples of the cell-pillar interaction are presented in Fig. S5 extracted from Video S2. We define a contact zone around each pillar as the region within a distance δ from the pillar surface (see Fig. 5 *a*) and define a contact event when a cell surface enters this zone. We measure the contact time τ_c as the time spent by a cell in a contact zone in each contact event (a contact event occurs when the distance between the cell nucleus and the center position of the pillar falls below the sum of the cell radius, δ, and the pillar radius). For different choices of δ, we measure τ_c for all cell trajec-
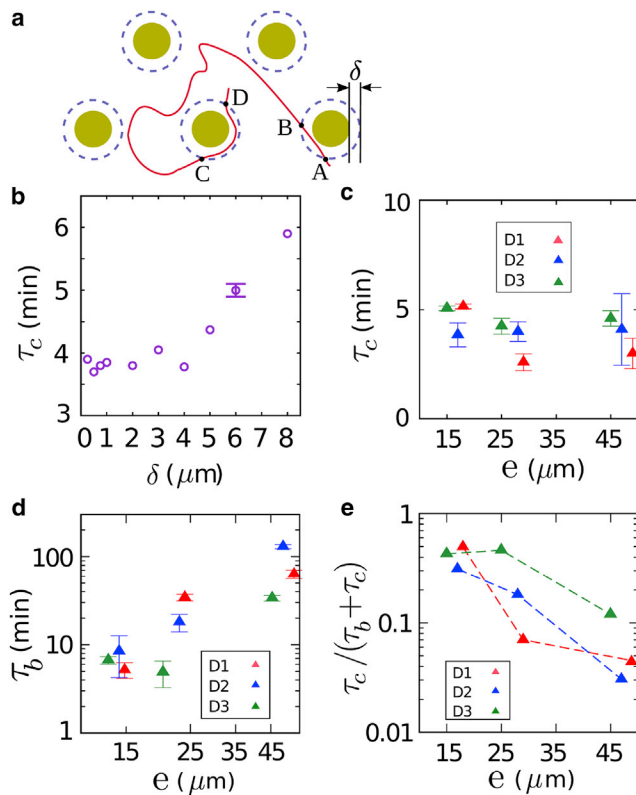

FIGURE 5 (*a*) Schematic example of a cell trajectory that visits the contact zones twice. The corresponding contact times τ_c are $t_{A \to B}$ and $t_{C \to D}$, and it spends $\tau_b = t_{B \to C}$ in the bulk. The dashed circles indicate the borders of the contact zones, with the contact distance δ from the pillar surfaces. (*b*) Contact time τ_c versus the thickness δ of the contact zone for device D3 with $e = 45$ μm. The single error bar represents the typical estimated errors for all data. (*c*–*e*) Mean contact time τ_c (*c*), mean bulk time τ_b (*d*), and the fraction of time spent in the vicinity of pillars $\frac{\tau_c}{\tau_c + \tau_b}$ (*e*) versus pillar spacing *e* for different chambers. The error bars in (*c*) and (*d*) indicate the standard deviation. (*d*) and (*e*) are presented in log-log and log-lin scales, respectively. The numbers of independent experiments and analyzed tracks are the same as in Fig. 2. To see this figure in color, go online.

tories belonging to each chamber. The typical result is presented in Fig. 5 *b* for device D3 with $e = 45$ μm. It can be seen that below a critical distance $\delta_c \approx 4$ μm, the contact time τ_c is independent of the choice of δ, evidencing the formation of the cell-pillar contact. We choose a contact distance $\delta = 2$ μm within the plateau regime (i.e., $\delta < \delta_c$) for all chambers and measure the resulting contact time τ_c in different experiments. The resulting mean contact time τ_c is around 3.9 $\pm$ 0.2 min for all chambers, independent of *h* or *e* (Fig. 5 *c*).

We similarly introduce a bulk time τ_b as the duration of time that a cell spends in the bulk of the pillar forest between two successive contact events. The mean value of the bulk time τ_b is presented in Fig. 5 *d* for different chambers. τ_b reduces with decreasing *e* since the available bulk area decreases and the cells visit the pillars more frequently. In Fig. 5 *e*, the fraction of time spent in the vicinity of pillars is shown. This fraction increases with decreasing *e* as the relative contribution of the contact events increases.

We checked that the cell velocity *v* and persistence $\mathscr{R}$ in the vicinity of pillars do not differ significantly from their values in the bulk of the system. In general, however, the dynamics in the vicinity of obstacles can be different from the bulk, depending on the nature of cell-obstacle interactions.

Numerical results

According to the results of the previous sections, the decrease of pillar spacing strengthens the trapping effect in local regions between neighboring pillars and also increases the frequency of cell-pillar contact events. Both effects reduce the cell diffusivity and decrease the diffusion constant *D*. To understand how the relative contributions of these two effects evolve with *e*, we perform simulations with and without cell-pillar contact times.

We model the migration of cells with a persistent random walk in a two-dimensional medium containing circular obstacles. The impact of the vertical confinement *h* is implicitly considered by the persistence $\mathscr{R}$ of the persistent random walker in our model. We first validate our numerical model by comparing it with the experimental data. For each experiment, the corresponding geometrical quantities *d*, *e*, and pillar positions are used as input for simulations. Persistent random walkers with velocity and turning-angle distributions compatible with each experiment (as presented in Fig. 2) are considered. For the interactions with pillars, two models are considered: 1) a model without a cell-pillar contact time, in which the walker experiences a specular reflection when hitting a pillar, and 2) a model with cell-pillar contact time, in which the random walker halts for a mean contact time $\tau_c = 3.5$ min in the vicinity of pillars, when it enters a contact zone with $\delta = 2$ μm, compatible with the results of the previous subsections. The details of the simulation method are presented in the materials and methods section. We obtain the time evolution of the

MSD. From the asymptotic regime of the MSD, we extract the diffusion constant D as a key parameter that represents the diffusivity in arrangements of obstacles (24–32,53) and is conversely related to the first-passage time of the walker (54–56). To compare the numerically obtained MSD with the experimental results, as a typical example, we present the results for the experiment (D2, T2) in Fig. 6 a. The result of the simulation with empirical input matches very well with the experimental data, but the model without a cell-pillar contact time leads to a larger MSD. We checked that the simulations satisfactorily capture the time evolution of the MSD in other chambers as well.

In order to gain more insight into the dependence of cell diffusivity on the pillar spacing, we perform Monte Carlo simulations of a walker with a diffusive dynamic ($\mathscr{R} = 0$) and mean velocity of 3.5 μm/min, with and without being temporarily captured by the pillars at the cell-pillar contact events. Fig. 6 b shows that the impact of the cell-pillar contact time on D is more pronounced at smaller pillar spacing. The experimental results with $\mathscr{R} \simeq 0$ are also presented in Fig. 6 b, which show a satisfactory agreement with simulations. See Fig. S6 for a comparison between the numerical and experimental results at other persistence values $\mathscr{R} \neq 0$.

DISCUSSION

We have studied the in vitro ameboid migration of HL-60 cells differentiated into neutrophils in quasi-two-dimensional confined geometries containing regularly arranged cylindrical micropillars. The distance between the parallel plates and the spacing between pillars have been varied to study their impact on the cell dynamics. To achieve a pure
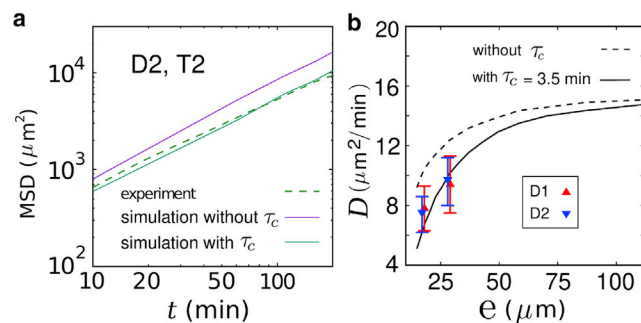

FIGURE 6 (*a*) Time evolution of the MSD in the asymptotic regime. A comparison is made between the results of experiments and simulations. An ensemble of 10^5 random walkers is chosen in the simulations. The numbers of independent experiments and analyzed tracks are given in the caption of Fig. 2. The experimental conditions of each device are mimicked in the simulations. (*b*) Diffusion constant D versus pillar spacing e obtained from simulations with $\mathscr{R} = 0$ and mean velocity $v = 3.5$ μm/min. The difference between the results of the simulations with and without cell-pillar contact times grows with decreasing e. The symbols represent the diffusion constant of cells in experiments with devices (D1, T2) and (D2, T3), whose persistence and velocity are $\mathscr{R} \simeq 0$ and $v \simeq 3.5$ μm/min. The error bars represent the standard deviation. To see this figure in color, go online.

ameboid migration, we have used coating with poly-L-lysine grafted with PLL-PEG, which prevents the cell-environment adhesion (14,16,57). In general, the cell dynamics can be affected by other coatings, as they may lead to different levels of adhesion and a mixture of ameboid and mesenchymal migration modes. As the goal has been to understand the effects of the vertical confinement h and the pillar spacing e on the cell dynamics, we have varied h from device D1 to D3 and the pillar spacing e in each device within the technically possible range for us. Constructing a control device without pillars leads to chamber collapse with our fabrication techniques, thus the presence of a minimum number of pillars was inevitable (corresponding to $e \sim 45$–50 μm).

So far, there has been very little experimental information on how vertical confinement influences ameboid cell migration. While reduction of cell velocity upon further squeezing the cell was reported in (38), here we observe that the velocity of differentiated HL-60 cells (with a typical size of $L \sim 10$ μm) is interestingly not affected when squeezed from $h = 6$ μm to even $h = 3.5$ μm. In contrast, the persistence reduces: the cells move persistently at $h = 6$ μm but just diffuse at $h = 3.5$ μm. Thus, an important message of the present study is that while cells are able to preserve their velocity under strong confinement, they lose the ability to control their direction of motion. These results are in agreement with our recent findings that the ability of migrating cells to maintain their velocity or direction of motion is unequal (58).

Another goal of the present study has been to understand how the lateral confinement imposed by pillars influences the ameboid migration. We note that the regime of strong lateral confinement was previously studied in similar pillar forests (5–7,20). In this regime, the pillar spacing is smaller than the cell size, thus the cell is often in simultaneous contacts with several pillars and benefits from a directed pillar-to-pillar fast type of motion. Our single device D4 falls into this category. We observe that in this device, the cells are significantly faster, with a mean velocity $v = 5.01 \pm 0.02$ μm/min. Also, looking at typical cell trajectories in Fig. S4 b reveals that the cells can benefit from the dense pillar arrangement in this regime to maintain the direction of motion over longer distances. Nevertheless, we are interested in the weak lateral confinement regime, where the pillars act as scatterers and randomize the cell trajectory. While this regime has been poorly studied, understanding the cell migration under weak lateral confinement is of importance toward the design of topotaxis devices and other practical applications. In devices D1 to D3, we kept the pillar spacing larger than the typical cell size to ensure that the cell cannot be in simultaneous contact with more than one pillar.

In the weak lateral confinement regime, decreasing the pillar spacing e reduces the diffusion constant D. We identify two responsible mechanisms: 1) decreasing e increases the mean escape time of cells from effective local traps between neighboring pillars and also decreases the cell

persistence due to scattering from pillars (30,32), and 2) we observe that the cells spend a finite time near pillar surfaces (such contact times have been previously reported for ameboid migration (5,20), though at highly dense regimes of pillars). The cell-pillar contacts slow the cell dynamics down and reduce D. By decreasing e, the frequency of cell-pillar contacts increases; thus, D further decreases. By means of numerical simulations with and without cell-pillar contact time τ_c, we have clarified the relative contributions of these two effects. The results in Fig. 6 b show that the impact of cell-pillar contacts on D is more pronounced at smaller pillar spacing. In this limit, the presence of τ_c reduces D even to half, which means that scattering from pillars and being temporarily captured by them contribute equally to reduce diffusivity.

We investigated the role of confinement and crowding on the ameboid cell migration. Our results highlight the differences between the nature of cell-obstacle interactions at low and high obstacle density regimes and its impact on the cell dynamics. We have also shown that squeezing the cells affects their velocity and persistence differently. Altogether, these findings can help to better understand the ameboid cell migration under more complicated topographic conditions. The results can be exploited to design in vitro assays for topotactic guidance of ameboid cells by tuning the degrees of confinement and crowding.

SUPPORTING MATERIAL

Supporting material can be found online at https://doi.org/10.1016/j.bpj. 2022.10.030.

AUTHOR CONTRIBUTIONS

ACKNOWLEDGMENTS

DECLARATION OF INTERESTS

The authors declare no conflict of interest.

REFERENCES

1. Heuzé, M. L., P. Vargas, …, A.-M. Lennon-Duménil. 2013. Migration of dendritic cells: physical principles, molecular mechanisms, and functional implications. *Immunol. Rev.* 256:240–254.

2. Aman, A., and T. Piotrowski. 2010. Cell migration during morphogenesis. *Dev. Biol.* 341:20–33.

3. Yamada, K. M., and M. Sixt. 2019. Mechanisms of 3D cell migration. *Nat. Rev. Mol. Cell Biol.* 20:738–752.

4. Park, J., D.-H. Kim, and A. Levchenko. 2018. Topotaxis: a new mechanism of directed cell migration in topographic ECM gradients. *Biophys. J.* 114:1257–1263.

5. Wondergem, J. A. J., M. Mytiliniou, …, D. Heinrich. 2021. Chemotaxis and topotaxis add vectorially for amoeboid cell migration. Preprint at bioRxiv. https://doi.org/10.1101/735779.

6. Reversat, A., F. Gaertner, …, M. Sixt. 2020. Cellular locomotion using environmental topography. *Nature.* 582:582–585.

7. Gorelashvili, M., M. Emmert, …, D. Heinrich. 2014. Amoeboid migration mode adaption in quasi-3D spatial density gradients of varying lattice geometry. *New J. Phys.* 16:075012.

8. Frey, M. T., I. Y. Tsai, …, Y. L. Wang. 2006. Cellular responses to substrate topography: role of myosin II and focal adhesion kinase. *Biophys. J.* 90:3774–3782.

9. Kaiser, J.-P., A. Reinmann, and A. Bruinink. 2006. The effect of topographic characteristics on cell migration velocity. *Biomaterials.* 27:5230–5241.

10. Muthinja, M. J., J. Ripp, …, F. Frischknecht. 2017. Microstructured blood vessel surrogates reveal structural tropism of motile malaria parasites. *Adv. Healthc. Mater.* 6:1601178.

11. Hawkins, R. J., M. Piel, …, R. Voituriez. 2009. Pushing off the walls: a mechanism of cell motility in confinement. *Phys. Rev. Lett.* 102:058103.

12. Lämmermann, T., B. L. Bader, …, M. Sixt. 2008. Rapid leukocyte migration by integrin-independent flowing and squeezing. *Nature.* 453:51–55.

13. Chabaud, M., M. L. Heuzé, …, A. M. Lennon-Duménil. 2015. Cell migration and antigen capture are antagonistic processes coupled by myosin II in dendritic cells. *Nat. Commun.* 6:7526.

14. Maiuri, P., J.-F. Rupprecht, …, R. Voituriez. 2015. Actin flows mediate a universal coupling between cell speed and cell persistence. *Cell.* 161:374–386.

15. Shaebani, M. R., R. Jose, …, F. Lautenschläger. 2020. Persistence-speed coupling enhances the search efficiency of migrating immune cells. *Phys. Rev. Lett.* 125:268102.

16. Stankevicins, L., N. Ecker, …, F. Lautenschläger. 2020. Deterministic actin waves as generators of cell polarization cues. *Proc. Natl. Acad. Sci. USA.* 117:826–835.

17. Prentice-Mott, H. V., C.-H. Chang, …, J. V. Shah. 2013. Biased migration of confined neutrophil-like cells in asymmetric hydraulic environments. *Proc. Natl. Acad. Sci. USA.* 110:21006–21011.

18. Lautenschläger, F., S. Paschke, …, J. Guck. 2009. The regulatory role of cell mechanics for migration of differentiating myeloid cells. *Proc. Natl. Acad. Sci. USA.* 106:15696–15701.

19. Molino, D., S. Quignard, …, J. Fattaccioli. 2016. On-chip quantitative measurement of mechanical stresses during cell migration with emulsion droplets. *Sci. Rep.* 6:29113.

20. Arcizet, D., S. Capito, …, D. Heinrich. 2012. Contact-controlled amoeboid motility induces dynamic cell trapping in 3D-microstructured surfaces. *Soft Matter.* 8:1473–1481.

21. Kantsler, V., J. Dunkel, …, R. E. Goldstein. 2013. Ciliary contact interactions dominate surface scattering of swimming eukaryotes. *Proc. Natl. Acad. Sci. USA.* 110:1187–1192.

22. Lushi, E., V. Kantsler, and R. E. Goldstein. 2017. Scattering of biflagellate microswimmers from surfaces. *Phys. Rev. E.* 96:023102.

23. Contino, M., E. Lushi, …, M. Polin. 2015. Microalgae scatter off solid surfaces by hydrodynamic and contact forces. *Phys. Rev. Lett.* 115:258102.

24. Saxton, M. J. 1982. Lateral diffusion in an archipelago: effects of impermeable patches on diffusion in a cell membrane. *Biophys. J.* 39:165–173.

25. Saxton, M. J. 1987. Lateral diffusion in an archipelago: the effect of mobile obstacles. *Biophys. J.* 52:989–997.

26. Saxton, M. J. 1989. Lateral diffusion in an archipelago: distance dependence of the diffusion coefficient. *Biophys. J.* 56:615–622.

27. Saxton, M. J. 1993. Lateral diffusion in an archipelago: single-particle diffusion. *Biophys. J.* 64:1766–1780.

28. Saxton, M. J. 1996. Anomalous diffusion due to obstacles: a Monte Carlo study. *Biophys. J.* 70:1250–1262.

29. Saxton, M. J. 1993. Lateral diffusion in an archipelago: dependence on tracer size. *Biophys. J.* 64:1053–1062.

30. Machta, J., and R. Zwanzig. 1983. Diffusion in a periodic Lorentz gas. *Phys. Rev. Lett.* 50:1959–1962.

31. Sadjadi, Z., M. Miri, …, S. Nakhaee. 2008. Diffusive transport of light in a two-dimensional disordered packing of disks: analytical approach to transport mean free path. *Phys. Rev. E Stat. Nonlin. Soft Matter Phys.* 78:031121.

32. Dagdug, L., M.-V. Vazquez, …, S. M. Bezrukov. 2012. Diffusion in the presence of cylindrical obstacles arranged in a square lattice analyzed with generalized Fick-Jacobs equation. *J. Chem. Phys.* 136:204106.

33. Spagnolie, S. E., G. R. Moreno-Flores, …, E. Lauga. 2015. Geometric capture and escape of a microswimmer colliding with an obstacle. *Soft Matter.* 11:3396–3411.

34. Jakuszeit, T., O. A. Croze, and S. Bell. 2019. Diffusion of active particles in a complex environment: role of surface scattering. *Phys. Rev. E.* 99:012610.

35. Sipos, O., K. Nagy, …, P. Galajda. 2015. Hydrodynamic trapping of swimming bacteria by convex walls. *Phys. Rev. Lett.* 114:258104.

36. Zhou, X., R. Zhao, …, B. Qu. 2017. Bystander cells enhance NK cytotoxic efficiency by reducing search time. *Sci. Rep.* 7:44357.

37. Shaebani, M. R., L. Stankevicins, …, F. Lautenschläger. 2022. Effects of vimentin on the migration, search efficiency, and mechanical resilience of dendritic cells. *Biophys. J.* 121:3950–3961. https://doi.org/10.1016/j.bpj.2022.08.033.

38. Yip, A. K., K.-H. Chiam, and P. Matsudaira. 2015. Traction stress analysis and modeling reveal that amoeboid migration in confined spaces is accompanied by expansive forces and requires the structural integrity of the membrane–cortex interactions. *Integr. Biol.* 7:1196–1211.

39. Shaebani, M. R., H. Rieger, and Z. Sadjadi. 2022. Kinematics of persistent random walkers with two distinct modes of motion. *Phys. Rev. E.* 106:034105.

40. Elgeti, J., and G. Gompper. 2015. Run-and-tumble dynamics of self-propelled particles in confinement. *EPL.* 109:58003.

41. Hafner, A. E., L. Santen, …, M. R. Shaebani. 2016. Run-and-pause dynamics of cytoskeletal motor proteins. *Sci. Rep.* 6:37162.

42. Pinkoviezky, I., and N. S. Gov. 2013. Transport dynamics of molecular motors that switch between an active and inactive state. *Phys. Rev. E Stat. Nonlin. Soft Matter Phys.* 88:022714.

43. Shaebani, M. R., and H. Rieger. 2019. Transient anomalous diffusion in run-and-tumble dynamics. *Front. Phys.* 7:120.

44. Theves, M., J. Taktikos, …, C. Beta. 2013. A bacterial swimmer with two alternating speeds of propagation. *Biophys. J.* 105:1915–1924.

45. Hauert, A. B., S. Martinelli, …, V. Niggli. 2002. Differentiated HL-60 cells are a valid model system for the analysis of human neutrophil migration and chemotaxis. *Int. J. Biochem. Cell Biol.* 34:838–854.

46. Collins, S. J., F. W. Ruscetti, …, R. C. Gallo. 1979. Normal functional characteristics of cultured human promyelocytic leukemia cells (HL-60) after induction of differentiation by dimethylsulfoxide. *J. Exp. Med.* 149:969–974.

47. Renkawitz, J., A. Reversat, …, M. Sixt. 2018. Chapter 5 - micro-engineered "pillar forests" to study cell migration in complex but controlled 3D environments. *In* Microfluidics in Cell Biology Part B: Microfluidics in Single Cells. M. Piel, D. Fletcher, and J. Doh, eds Academic Press, pp. 79–91, volume 147 of Methods in Cell Biology.

48. Sadjadi, Z., M. R. Shaebani, …, L. Santen. 2015. Persistent-random-walk approach to anomalous transport of self-propelled particles. *Phys. Rev. E Stat. Nonlin. Soft Matter Phys.* 91:062715.

49. Sadjadi, Z., and M. R. Shaebani. 2021. Orientational memory of active particles in multistate non-Markovian processes. *Phys. Rev. E.* 104:054613.

50. Landau, L. D., and E. M. Lifshitz. 1958. Statistical Physics. Pergamon Press.

51. Doi, M., and S. F. Edwards. 1986. The Theory of Polymer Dynamics. Oxford University Press.

52. Shaebani, M. R., Z. Sadjadi, …, L. Santen. 2014. Anomalous diffusion of self-propelled particles in directed random environments. *Phys. Rev. E Stat. Nonlin. Soft Matter Phys.* 90:030701.

53. Tierno, P., and M. R. Shaebani. 2016. Enhanced diffusion and anomalous transport of magnetic colloids driven above a two-state flashing potential. *Soft Matter.* 12:3398–3405.

54. Condamin, S., O. Bénichou, and M. Moreau. 2005. First-passage times for random walks in bounded domains. *Phys. Rev. Lett.* 95:260601.

55. Bénichou, O., M. Coppey, …, R. Voituriez. 2005. Optimal search strategies for hidden targets. *Phys. Rev. Lett.* 94:198101.

56. Redner, S. 2001. A Guide to First-Passage Processes. Cambridge University Press, Cambridge.

57. Liu, Y.-J., M. Le Berre, …, M. Piel. 2015. Confinement and low adhesion induce fast amoeboid migration of slow mesenchymal cells. *Cell.* 160:659–672.

58. Shaebani, M. R., M. Piel, and F. Lautenschläger. 2022. Distinct speed and direction memories of migrating dendritic cells diversify their search strategies. *Biophys. J.* 121:4099–4108. https://doi.org/10.1016/j.bpj.2022.09.033.